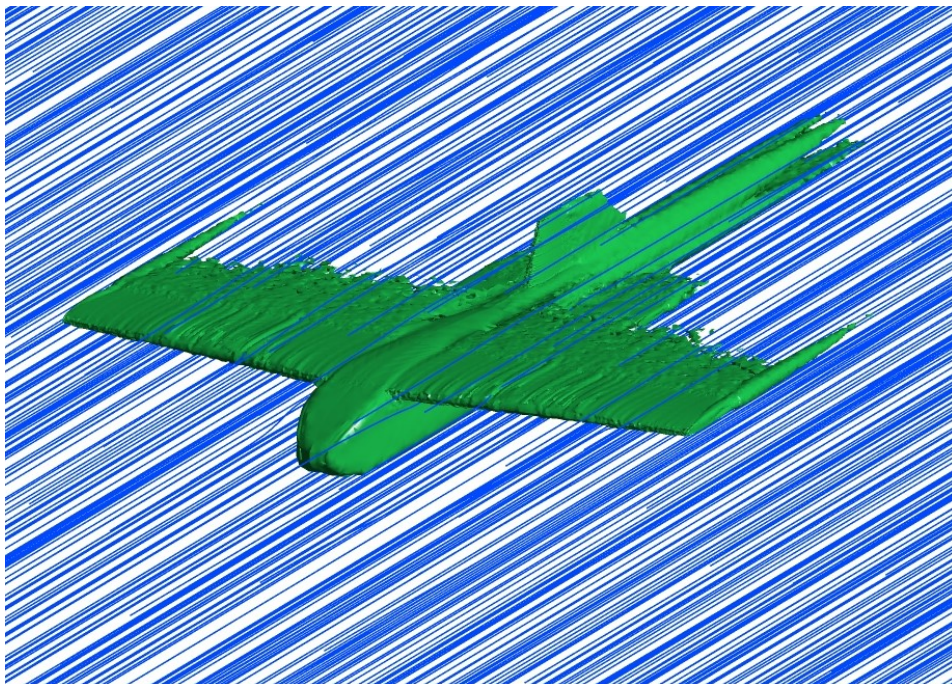# Aerodynamic Analysis of an Unmanned Aerial Vehicle - MERAYU

Bharath Kumar Kuna (bhaku277)

Meet Akhilkumar Agrawal (meeag462)

Rohit Raja (rohra521)

Yuvarajendra Anjaneya Reddy (yuvan983)

Nomenclature

Abbreviations and Acronyms

Abbreviation	Meaning
AoA	Angle of Attack
AR	Aspect Ratio
BLT	Boundary Layer Thickness
CFD	Computational Fluid Dynamics
C_D	Coefficient of Drag
C_f	Coefficient of skin-friction
C_L	Coefficient of Lift
FMG	Full Multi Grid
HT	Horizontal Tail
MAC	Mean Aerodynamic Chord (m)
NACA	National Advisory Committee for Aeronautics
RANS	Reynolds Averaged Navier-Stokes
Re	Reynolds number
UAV	Unmanned Aerial Vehicle

Latin Symbols

Symbol	Description	Units
U	Velocity	$\left[m \ s^{-1}\right]$
L	Characteristic length	$[m]$
C_L	Coefficient of lift	$[-]$
C_D	Coefficient of drag	$[-]$
C_f	Coefficient of skin-friction	$[-]$
AoA	Angle of attack	$[°]$
du/dy	Velocity gradient in Y direction	$\left[s^{-1}\right]$

Greek Symbols

Symbol	Description	Units
ρ	Density	$\left[kg \ m^{-3}\right]$
α	Angle of attack	$[°]$
μ	Dynamic viscosity	$[Pa-s]$

Contents

1 Introduction

A fully functional prototype UAV was previously developed for the purpose of medical payload transport which could carry payloads upto 4 kgs and fly for more than 100 kms. The UAV was designed with a minimalist approach consisting of a cubical fuselage as it would allow more space utilisation inside the fuselage. The UAV features a rectangular un-swept wing mounted in a high wing configuration. The airfoil used for the main wing is NACA 2410, while that for the empennage is NACA 0012. The UAV was propelled with the help of two wing mounted motors with propellers and lastly, a conventional empennage has been chosen to provide yaw and pitch moments. Dimensional specifications of the UAV are addressed in Table. 4 on a scale of the 1:1 prototype. This UAV is designed and developed with the intentions of carrying medical supplies to remote areas where accessibility is an issue. With the help of this UAV, it is possible to deliver First Aid using parachute drops in hilly, rural, under-developed regions.

Specifications	Value
Wing Span	1.82 m
Length	1.234 m
Wing AR	7
Wing Root Chord	0.318 m
Horizontal Tail Span	0.56 m
Horizontal Tail AR	3
Vertical Tail	0.23 m
Vertical Tail AR	1.5
Mean Aerodynamic Chord	0.273 m

Table 4: MERAYU Specifications

To accomplish this task efficiently, a detailed analysis of external aerodynamics of the UAV has to be performed to carefully understand the flow patterns and assess the aerodynamic performance. External aerodynamic analysis is a significant way for the development of an aircraft as it helps to analyze the flow over the subject by implementing a CFD approach and perform suitable design modifications, which further improves the aerodynamic efficiency. This in turn translates to the UAV being capable of achieving higher range, cruise speed, cruise altitude, etc. Hence, it becomes highly essential to study the airflow over the aircraft in detail. To carry out this kind of evaluations, wind tunnel testing would be an ideal and most accurate option, but also highly expensive. Therefore it becomes logical to take advantage of the computational tool and resources available to arrive at credible results. In this project, ANSYS FLUENT 19.2 and 2019R2 have been utilised as the computational tool, whereas the geometry has been designed and simplified in CATIA-V5 and Design modeler is used to generate the domain and the body of influences.

During the flight test, the pilot had reported inefficiency of the elevator even though the elevator had been sized appropriately. The cause is then narrowed down to type of empennage configuration, which lies in the turbulent downwash of the wing and thereby affecting the maneuverability of the aircraft. This greatly minimised

the efficiency of the elevator. Thus, the effect of the main wing downwash is also being studied by looking at the aerodynamic performance of the horizontal tail.

1.1   Aim and scope of the work

Thus, with the pilot inputs, the main aim of the work includes an external aerodynamic study of the aircraft along with the horizontal tail performance to determine the underlying problem by performing simulations over a range of angles of attacks with the help of the computational tools and resources available.

The work-flow process addresses the study of external aerodynamics of a designed scaled-down geometry and also to observe the nature of flow over the aircraft. If time permits, these results will be utilized in order to make design changes which can improve the aerodynamic performance.

2   Methods

The following steps are implemented to achieve the intended project goals:

2.1   Pre-processing

- The 3D aircraft geometry is being imported via the product file generated using CATIA-V5, and the required external fluid domain is being generated. A domain with C-type inlet is utilized to simulate the flow over the aircraft. In external aerodynamic problems, the domain should be large enough to ensure that there is no influence of the walls to the flow physics acting around the body of interest[1]. Hence, a domain with 6 aircraft lengths in the front, 17 aircraft lengths at the rear, and 10 aircraft lengths on all other sides is generated. Next, the body of influences for the refinements, around the aircraft component parts, to be made in the mesh are generated. Also, since the 3D object is symmetric with respect to vertical plane along the longitudinal axis, the study is being performed on a symmetric domain, thereby also reducing the computational cost by a significant margin.

- Meshing of the geometry is performed using the ANSYS meshing tool. Tetrahedral mesh elements are used as the mesh element type, since this element type is more suitable for complex geometrical features[2], like that of an aircraft. Refinements techniques like Face Sizing, Edge sizing, Body of influence, and Inflation layers have been implemented for meshing.

  Face sizing is implemented to faces where the mesh quality seemed bad. Edge sizing is performed at all the trailing edges for the main wing, horizontal tail and the vertical tail to properly distribute the smaller elements at the edges by giving the number of divisions as the input. Twenty inflation layers, with first layer thickness as the control parameter are implemented to all the edges over the full aircraft. Since the near wall flow is of primary importance in this study, and also since the aerodynamic coefficients are measured on the aircraft faces. Different inflation zones were created by dividing the geometry in various parts like the wing, fuselage, horizontal tail and the vertical tail and maintain a $y+$ value of around 1, which can also be observed from Fig. 7.

  Separate bodies of influence are created for the fuselage, main wing, horizontal tail and the vertical tail to properly resolve the flow around them by varying the element size in the particular region. Also, a bigger body of influence is created around the aircraft body to capture the flow physics behaving around it.

  After meshing is being performed, the mesh is checked for quality parameters like Skewness, Element quality and Orthogonality, and further refinement is performed by implementing the appropriate refinement techniques based on the areas where mesh quality is insufficient. A rule of thumb for a good quality mesh is that the skewness value should be closer to 0, while orthogonality should be closer to 1[3].

For checking the mesh resolution at each step in the mesh independency study, firstly a mesh quality check is being performed for the values of parameters like Element Quality, Skewness and Orthogonality and can be observed from Table. 5. And if the mesh quality is found not sufficient enough, then refinement techniques are implemented in those regions as discussed before.

Mesh metric	Minimum	Average
Skewness	4.36e-07	0.213
Orthogonality	1.23e-03	0.785
Element Quality	5.92e-04	0.831

Table 5: Mesh quality check

The generated mesh can be observed from Fig. 1, while the created monitor points can be observed from Fig. 2. The monitor points placed are located at: one, in the wake region behind the main wing's trailing edge, the second at the wing-fuselage interaction, the third behind the vertical tail's trailing edge, and the fourth at the further aft of the aircraft. It has also been made sure that the transition of mesh elements from the inflation to the bulk mesh is smooth enough to avoid numerical discrepancies as can be observed from Fig. 1.
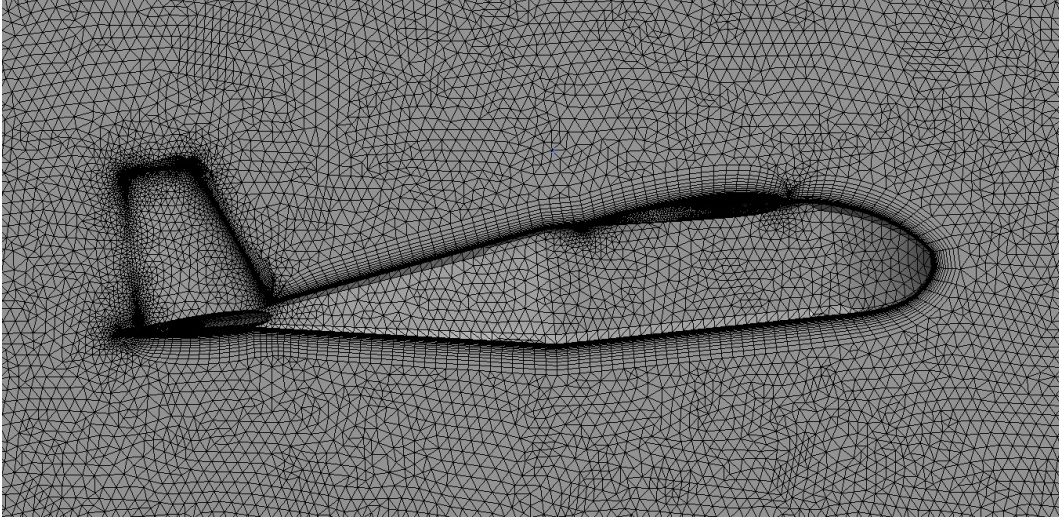
Figure 1: Mesh with tetrahedral elements and inflation layers

Also, to check how the performance of the Horizontal Tail (HT) is being affected by the flow over the wing and fuselage, an additional study is performed wherein simulations were ran with just the horizontal tail as the object inside the domain and a comparison of performance parameters between the horizontal tail with the aircraft and just the horizontal tail.
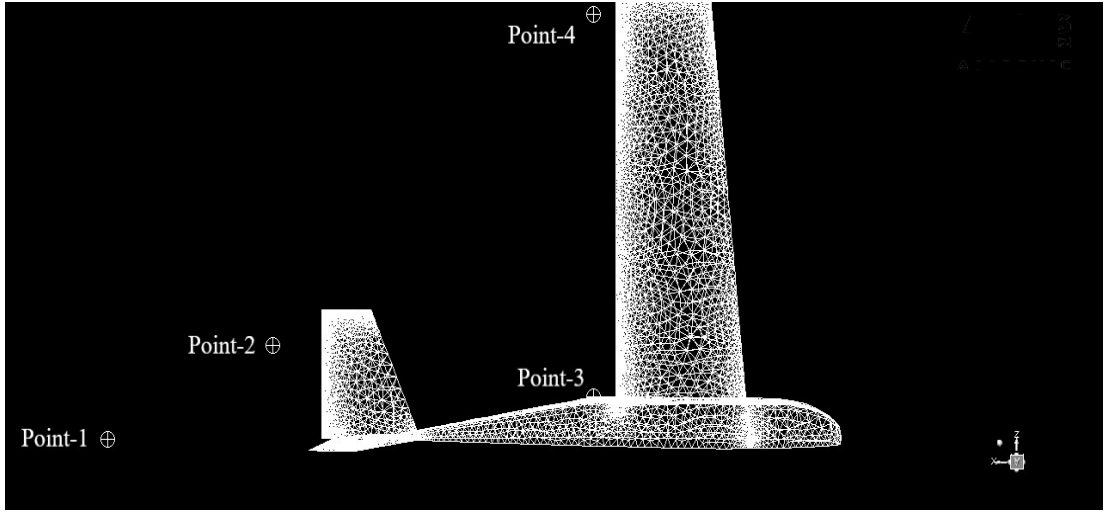
Figure 2: Monitor points setup around the aircraft

2.2 Setup

The flow is simulated for UAV cruising at 15 m/s at an altitude of 1000 m and all the dimensions are taken by scaling down the original geometry to a scale of 1:10. The dynamic viscosity and density corresponding to the altitude are 1.758e-05 $Pa - s$ and 1.112 kg/m^3 respectively. The Reynolds number based on the characteristic length of 0.0273 m (Mean aerodynamic chord of the main wing) is calculated by using Eq.1, and is calculated to be as 25900.

$$Re = \rho U L / \mu \tag{1}$$

The setting up of the flow physics involves the following steps:

- Specification of the type of solver used - Steady State Pressure-Based solver in this case. The reason being, the simulation are performed at velocities lesser than 0.3 Mach and hence incompressible. The energy equation is turned off as any form of heat transfer is not included in the current study.

- Defining the turbulence model used for the simulation - Spalart-Allmaras one equation model. It is a low-cost Reynolds-Averaged Navier-Stokes(RANS) model solving a transport equation for a modified kinematic turbyulent eddy viscosity. It is designed specifically for external aerodynamic applications involving wall-bounded flows[4], and the model provides good performance in boundary layer problems with adverse pressure gradients[5]. It embodies a relatively new class of one-equation models where it is not necessary to calculate a length scale related to the local shear layer thickness.[6]

- Defining the material properties - air in this case and the air properties are defined according to the values at the cruise altitude

- The cell-zone conditions, and checking that the domain is selected as fluid. Also, the reference conditions are defined based on the values in Table 6.

5

Reference parameters	Values
Area	$0.005521\ m^2$
Density	$1.112\ kg/m^3$
Length	$0.0273(m)$
Pressure	$0\ (Pa)$
Temperature	$288.16\ K$
Velocity	$15\ (m/s)$
Viscosity	$1.758\text{e-}05\ (kg/m - s)$
Ratio of specific heats	1.4

Table 6: Reference conditions

- Defining the boundary conditions for the various faces of the domain. The defined boundary conditions can be observed from Table 7.

Geometrical Entities	Boundary condition	Parameters	Value
Inlet	Velocity-Inlet	Velocity	15 m/s
Outlet	Pressure-Outlet	Gauge Pressure	0 Pa
Walls	No-Slip	Wall Roughness	0.05
Side wall	Specified Shear	X-component	0 Pa
		Y-component	0 Pa
		Z-component	0 Pa
Symmetry	Symmetry	-	-

Table 7: Boundary Conditions

The specified shear boundary condition to the side wall is defined since this condition acts as a free-slip condition.

- Defining of the solution methods is implemented according to the inputs specified in Table 8.

Pressure-Velocity Coupling	
Scheme	Coupled
Spatial Discretization	
Gradient	Least Squares Cell Based
Pressure	Standard
Momentum	Second Order Upwind
Modified Turbulent Viscosity	Second Order Upwind

Table 8: Solution Methods

The Coupled solver reduces the time to overall convergence, by as much as five times when compared to SIMPLE, by solving momentum and pressure-based continuity equations in a coupled manner. Although there is a slight increase in the associated memory requirements for using this solver, its benefits far outweigh the drawbacks.[7]

The least squares cell based method is used because the mesh is unstructured and this method is comparable to that of the node-based gradient (and both are much more superior compared to the cell-based gradient). However, it is less expensive to compute the least-squares gradient than the node-based gradient.[8]. For the tetrahedral mesh, the flow is not aligned with the mesh. Therefore second order schemes are implemented, which are more accurate.

- Residuals for the transport equations are not checked for convergence, since a lot of computational cost is required for tighter convergence. On the other hand it is made sure that the residuals decrease sufficiently enough and stabilise after running the simulation for a few number of iterations as can be observed from Fig. 9. Hence, a steady state solution is being monitored while running the simulation for higher number of iterations and concluded that the solution is converged. To observe the steady state solution, various parameters like the overall Lift Coefficient, the Drag Coefficient and velocity at the four monitor points shown in the Fig. 2 are utilized.

- The monitoring points are also plotted and reported while running the simulation.

- The type of initialization technique being employed for the solver plays a major role in deciding the computational cost of the simulation. Hence, to provide an initial solution which is close to the final solution, two initialization techniques, namely, Hybrid Initialization and Full Multigrid (FMG) Initilization are employed. Hybrid initialization is carried out to efficiently initialize the solution which is purely based on the simulation setup and the user need not specify any additional inputs for initialization. While, an initial and approximate solution is provided to the Fluent solver using the Full Multigrid (FMG) initialization, which is used for complex flow problems like external flow and turbo-machinery, and this initial solution comes at a minimum cost to the overall cost of the computational expense.

- The simulation is being run for 1200 iterations till a steady state solution is observed for the monitor points, and also until the solution variables residual decrease substantially and become stable for a longer time.

- With the same setup of the simulation used before, the mesh obtained from mesh independency obtained from the mesh independency study for 6° AoA is then utilised for different angle of attacks such as 3°, 0° and −3°, by rotating the geometry to carry out the further study.

2.3 Post-processing

Mesh sensitivity study is being conducted to observe how the results are varying with the number of mesh elements. The purpose of this study involves scraping out the errors obtained for the coarse meshes, so that more accurate results can be generated from highly resolved meshes. Finer mesh produces a change in the solution obtained, hence a state has to be achieved where there is no further change or negligible changes are observed in the solution, hence making the solution grid

7

independent. The refinement of the mesh is carried out by decreasing the mesh element size. But on the other hand, higher computation resources and time is required for obtaining such accurate results.

The study is performed by initially starting with one million elements, then the mesh is further refined to two million, four million, ten million, fourteen million and thirty-one million using the refinement techniques discussed before. The parameters used to check mesh independency were Coefficient of Lift(C_L), Coefficient of Drag(C_D) of the full aircraft, fuselage, wing, horizontal tail and vertical tail. The mesh is considered to be mesh independent when the difference between total C_L and C_D between two successive meshes are less than 0.3%. The mesh independency results for the u-velocity, skin friction, C_L and C_D can be observed from Fig. 3, Fig. 4 and Table 9, and it can be stated that very minimal variation is observed on further increasing the mesh size for the mesh with 14M as the number of elements. Therefore, it can be said that the mesh is mesh-independent for 14M, and all the further study is performed using this mesh.

This study is performed for 6° AoA, the reason being a steady state is observed for the monitored points. Also, another simulation carried out for 8° AoA indicated that a steady state solution is not achieved. Hence, a mesh independency study is performed for 6° AoA. Thereafter, the finalized mesh from mesh independence study is used for simulating lower angles of attack.

No. of mesh elements	C_L	% difference	C_D	% difference
1 M	0.2731	-	0.03391	-
2 M	0.2724	0.21	0.03334	1.68
4 M	0.2751	0.94	0.03351	0.51
10 M	0.2729	0.78	0.03271	2.34
14 M	0.2726	0.12	0.3265	0.18
31 M	0.2724	0.07	0.0325	0.36

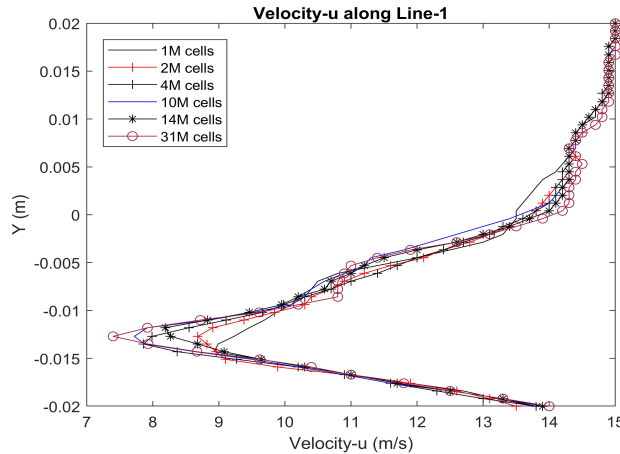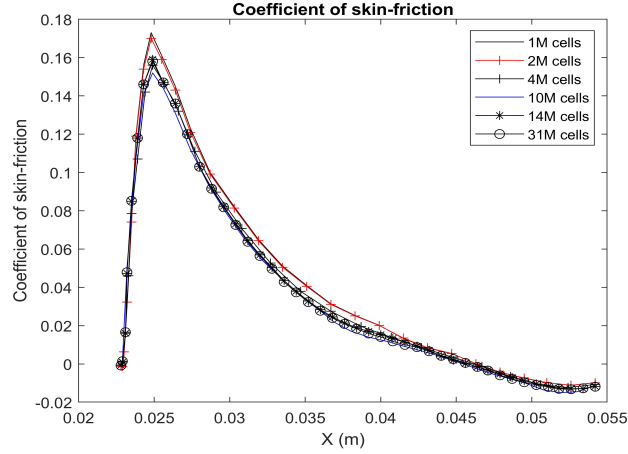Table 9: **Mesh independence study for C_L and C_D**

Figure 3: **Velocity u plotted against the vertical line for Mesh independence study**

Figure 4: Skin-friction coefficient plotted along the wing upper surface curvature for Mesh independence study

The report definitions are used to find Coefficients of lift and drag from the area average of lift and drag forces for fuselage, wing, horizontal tail and vertical tail. The wing C_L obtained is used to calculate lift induced drag. The difference between total C_D and the lift induced drag gives zero-lift drag. The contour of coefficient of pressure, velocity and streamlines will be used to analyze the flow physics. Also, an additional vertical line is being generated at the downstream side of the vertical tail along with a polyline (green-coloured) is being created at the boundary intersection of the symmetry and the wing plane; as can be observed from Fig. 5.
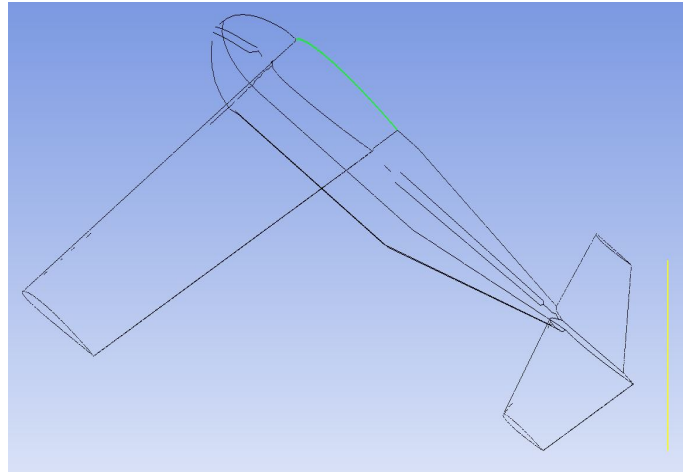
Figure 5: A vertical line and a polyline generated for post-processing purpose

To observe the vortical structures being formed due to the aircraft component shape, a visibility parameter 'Vortex core region' is generated located in the whole of fluid domain and can be observed from Fig. 18.

The performance comparison of the horizontal tail is performed by choosing the performance parameters as C_L Vs α and C_D Vs α curves for the full HT.

9

2.3.1   Theory for Boundary Layer Thickness

The part of the flow where the wall effects or slowing down of the fluid due to the viscosity is dominant and the existence of the velocity-gradient occurs, is known as the boundary layer. Inside the boundary layer, the momentum transfer of the fluid particles is transferred with the help of viscous effects which are sustaining shear stresses and transferring the disturbance of momentum from one fluid layer to the adjacent fluid layer along with the existence of the velocity gradients according to the Newton's law of viscosity as,

$$\tau = \mu \frac{du}{dy} \tag{2}$$

where, μ is the dynamic viscosity of the fluid, and du/dy is the velocity gradient normal to the wall.

A general definition to quantify the boundary layer thickness suggests that when the fluid velocity away from the wall starts to approach the free-stream velocity, then the region below it is known as the boundary layer region, and the appropriate boundary layer thickness can be calculated using the normal distance from the wall till it reaches the free-stream condition. This can be understood by implementing the following condition while plotting the u-velocity along the normal distance,

$$u - velocity \approx 0.99 u_\infty \tag{3}$$

where, u_∞ is the free-stream velocity. Inside of a turbuluent boundary layer, the fluid motion is very random and the kinetic energy of the fluid particles is very high. These high energy fluid particles produce more skin friction and high wall shear stresses, which thereby increase the friction drag produced on the aircraft. Also, when the pressure gradient along the flow direction rises abruptly, then due to this adverse change in pressure causes the flow to separate, as can be observed from Fig. 14, and hence creating low pressure regions known as the wake regions. These wake regions are responsible for increasing the pressure drag on the object. Hence, it is to be made sure that the boundary layer separation is moved further aft towards the trailing edge tip.

To check for the thickness of the boundary layer formation onto the main wing, three vertical lines, normal to the flow direction, are plotted such that one of the line is near the leading edge, the second line lies at 50% of the chord, and the third line lies at the aft towards the trailing edge of the wing MAC. These lines can be observed from Fig. 6.

2.3.2   Theory for Pressure Gradient

On the movement of a fluid particle on a curved or a cambered surface like that of an wing airfoil, a centripetal force acts on the fluid particle, due to the curvilinear surface of the the wing, and allows the fluid particle to change its direction of motion towards the center of curvature. This force is provided by the pressure gradients acting along the surface. Also, on the upper surface of the wing, the fluid particle experiences a stagnation point with very high pressure at the leading edge followed by lowering of the pressure towards the aft of the wing, and subsequently to ambient
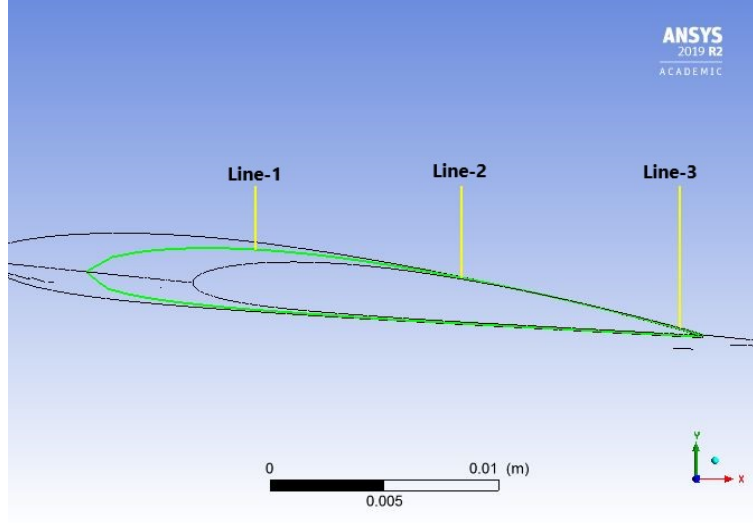
Figure 6: Plotting of the vertical lines at the wing MAC

pressure behind the wing[9]. Thus, a gradient is being generated due to the high camber side of the wing. To account for the pressure gradient acting on the surface in the airflow direction, a user-defined variable is defined with a Gradient method and Pressure as the parameter to observe the adverse pressure gradients resulting in flow separation.

The region where the fluid flows from low pressure to high pressure region, an adverse pressure gradient is observed and this sudden change is pressure is responsible for flow separation, which in turn increases the pressure drag on the aircraft caused due to the wake formation. The boundary layer theory and practical observations reveal that in a case where there is no pressure change in the airflow direction, the boundary layer does not separate and this is known as a favourable pressure gradient[10]. Thus, to avoid flow separation, it has to be made sure that the pressure gradient is favourable or zero over the surface.

To calculate the amount of separation from the wing surface, a wake area for each angle of attack is being created at a plane normal to MAC location of the main wing, where the wake area is plotted and quantified using the Iso-clip visibility parameter as follows,

$$uVelocity.GradientY <= 0 \tag{4}$$

and the wake area in the iso-clip is being quantified using a user-defined expression as can be observed below,

$$area@Iso\ Clip$$

Also, the amount of additional pressure drag being induced due to more separation is quantified and can be observed from Table. 11.

11

3 Results

3.1 Mesh Resolution

To check if the near-wall physics is being resolved or not, $y+$ value of each aircraft component is being checked for separately. The $y+$ value over the fuselage surface can be observed from Fig. 7. Similarly other aircraft components are checked for a $y+$ of around 1.
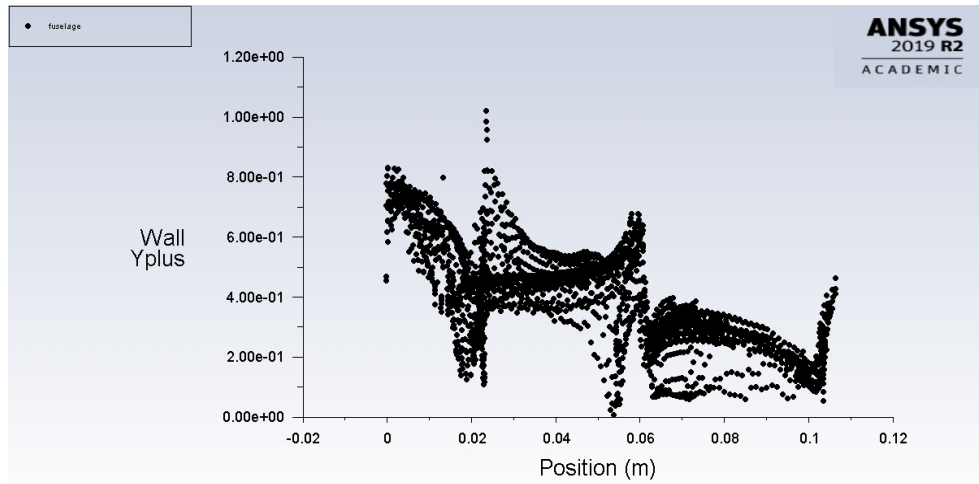

Figure 7: Wall $y+$ over the fuselage for the generated mesh

3.2 Solution Stability

The solution stability is checked for the velocity-magnitude at all the monitor points until the parameter levels-out/stabilises after obtaining a certain value, and can be observed from Fig. 8. Also, residuals are checked for a converged state as can be observed from Fig. 9.
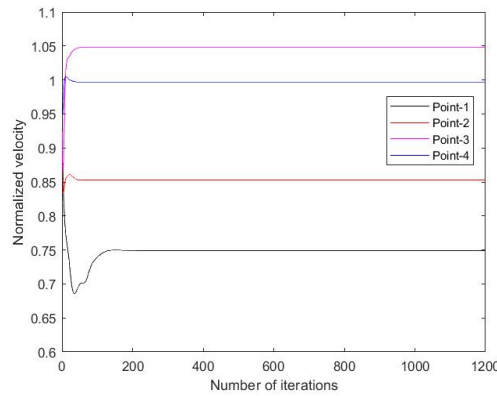
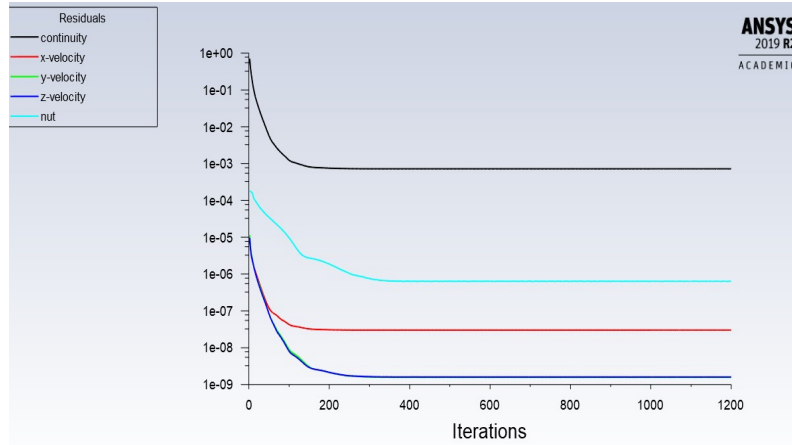
Figure 8: Solution stability for the monitor points

Figure 9: Residual stability

3.3 Aircraft Aerodynamic Performance

The aerodynamic performance of the aircraft is checked by plotting the aerodynamic coefficients at the wing MAC and can be observed from Fig. 10.
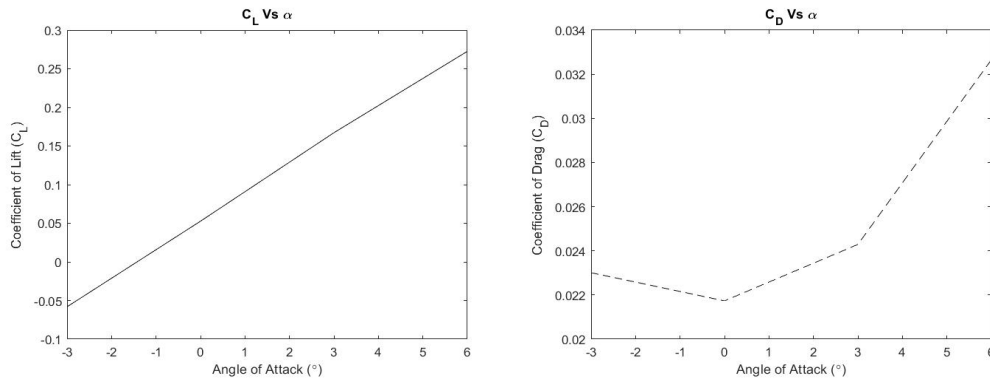

Figure 10: Aerodynamic coefficients for the aircraft

3.4 Boundary Layer Thickness and Turbulence

To quantify for the boundary layer thickness on the wing surface, u-velocity along the vertical lines created at the wing MAC, as can be observed from Fig. 6. The u-velocity plots can be at various locations for all angles of attacks can be observed from Fig. 11 and Fig. 12.
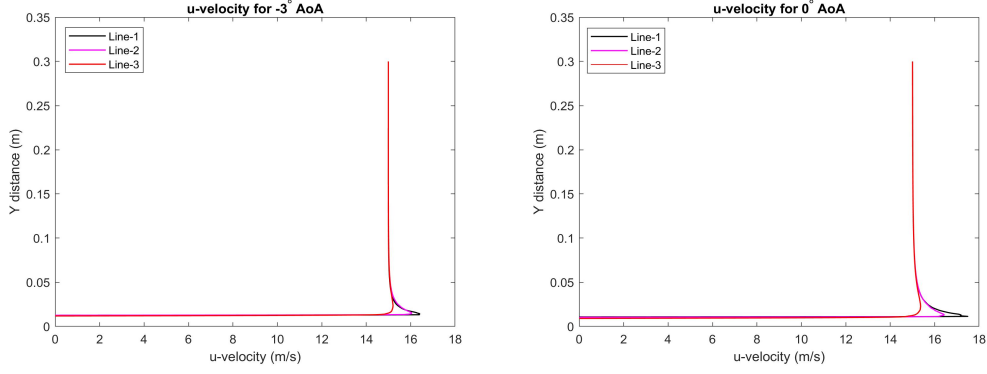
13

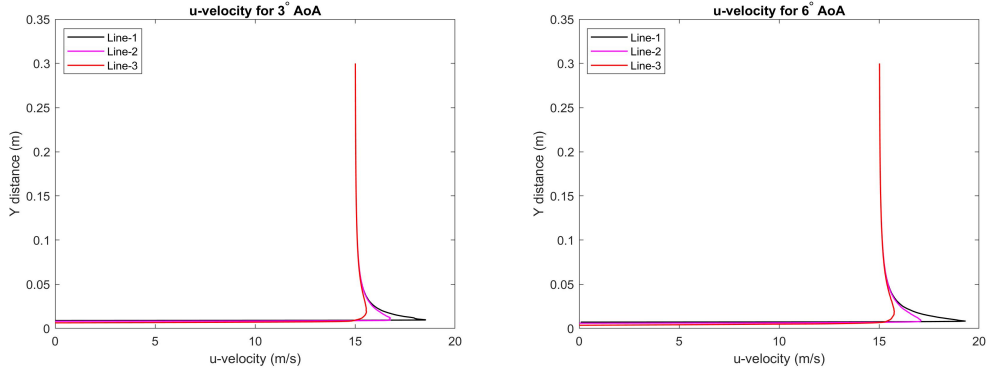**Figure 11: u-velocity along normal direction for $-3°$ and $0°$ AoA**

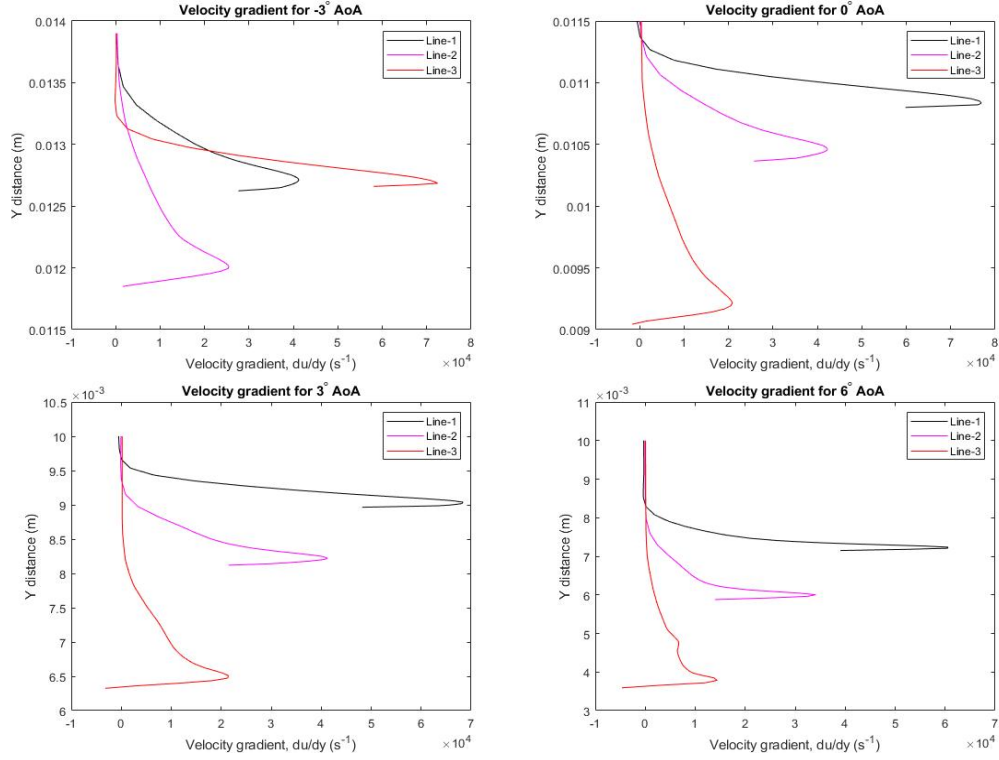**Figure 12: u-velocity along normal direction for $3°$ and $6°$ AoA**

Based on the results obtained for the u-velocity from Fig. 11 and Fig. 12, the boundary layer thickness (BLT) across the wing MAC on the 3 generated vertical lines can be observed from Table. 10 in accordance to the theory being discussed in section 2.3.1.

| AoA	BLT ($\times 10^{-2}$)[m]		
	Line-1	Line-2	Line-3
-3°	2.01	2.09	2.19
0°	4.05	4.17	4.28
3°	6.12	6.19	6.202
6°	7.88	8.00	8.01

Table 10: Boundary layer thickness

While to check for turbulence acting inside the boundary layer, the velocity gradient is being plotted as the variable along the lines in Fig. 6. The velocity gradients for all angles of attacks can be observed from Fig. 13.

Figure 13: Variation of velocity gradient along normal direction

A factor affecting the boundary layer separation from the wing's surface is the pressure gradient acting along the surface. The pressure gradient acting over the wing at the MAC location can be observed from Fig. 15. Also, to check for the flow separation from wing's surface, a wake area, as can be observed from Fig. 14, is being quantified based on the condition mentioned in equation 4. The red box in Fig. 14 indicates the wake area, and the picture to the right of it is the zoomed-in picture to get a clear idea of the wake formed. Also, the effect of the wake area to the induced contribution of the pressure in terms of pressure and viscous coefficients acting on the wing for various AoA's can be observed from Table. 11.
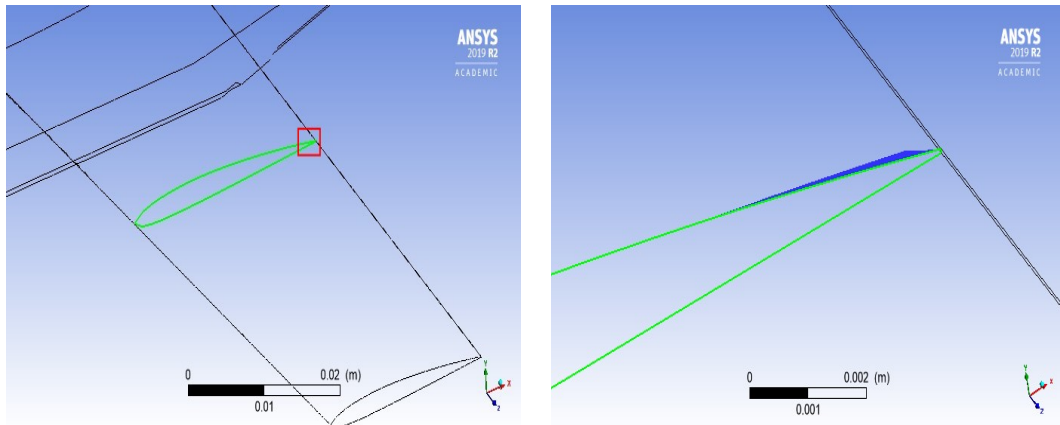
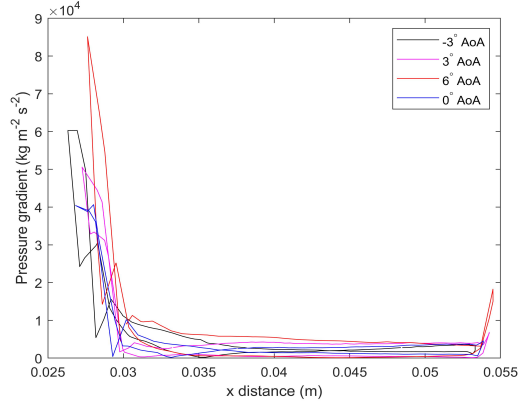**Figure 14: Wake area location on the wing MAC for $6°$ AoA**

Figure 15: Pressure gradient at the wing MAC

AoA	Area (m^2)	Pressure	Viscous	Drag Coefficient
$-3°$	7.27e-10	0.0061	0.0069	0.0131
$0°$	3.03e-08	0.0048	0.0079	0.0128
$3°$	7.48e-08	0.0078	0.0077	0.0156
$6°$	2.65e-07	0.0163	0.0067	0.0231

Table 11: Wake area at MAC for various AoA's using equation 4

3.5   Vortices Formation

To observe the vortical structures being formed around the aircraft due to its shape, parameters like velocity streamlines and vortex core regions are being implemented here.

The velocity streamlines are being plotted by creating planes normal to the aircraft face from the wing to the aft of the aircraft, and can be observed from Fig. 16 and Fig. 17.
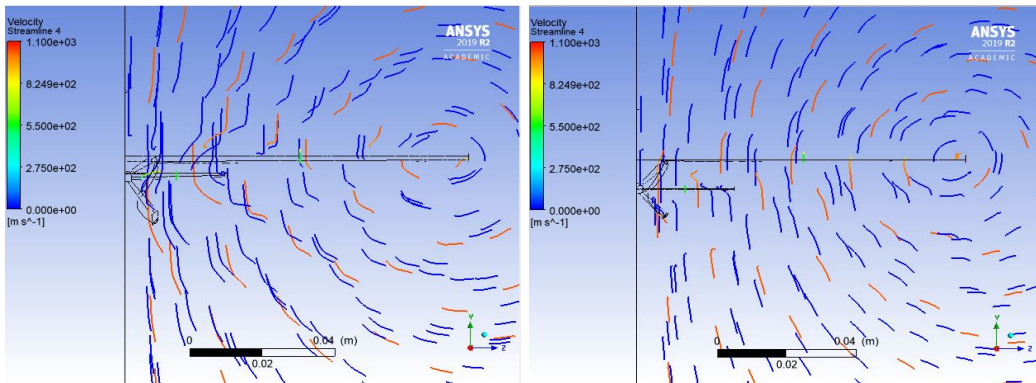

Figure 16: Velocity streamlines normal to aircraft face for $-3°$ and $0°$ AoA

While, to check for the vortex regions being generated from the aircraft surfaces, a vortex core region is being generated with Q-criterion as the parameter, and can be observed from Fig. 18.
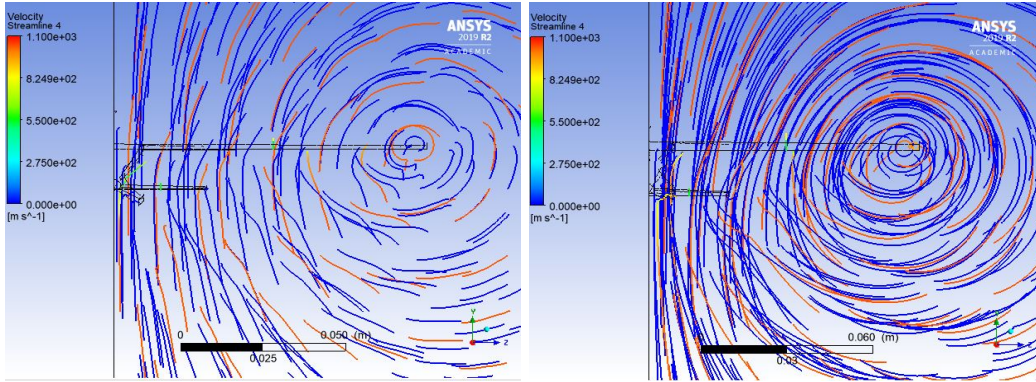
16

Figure 17: Velocity streamlines normal to aircraft face for $3°$ and $6°$ AoA
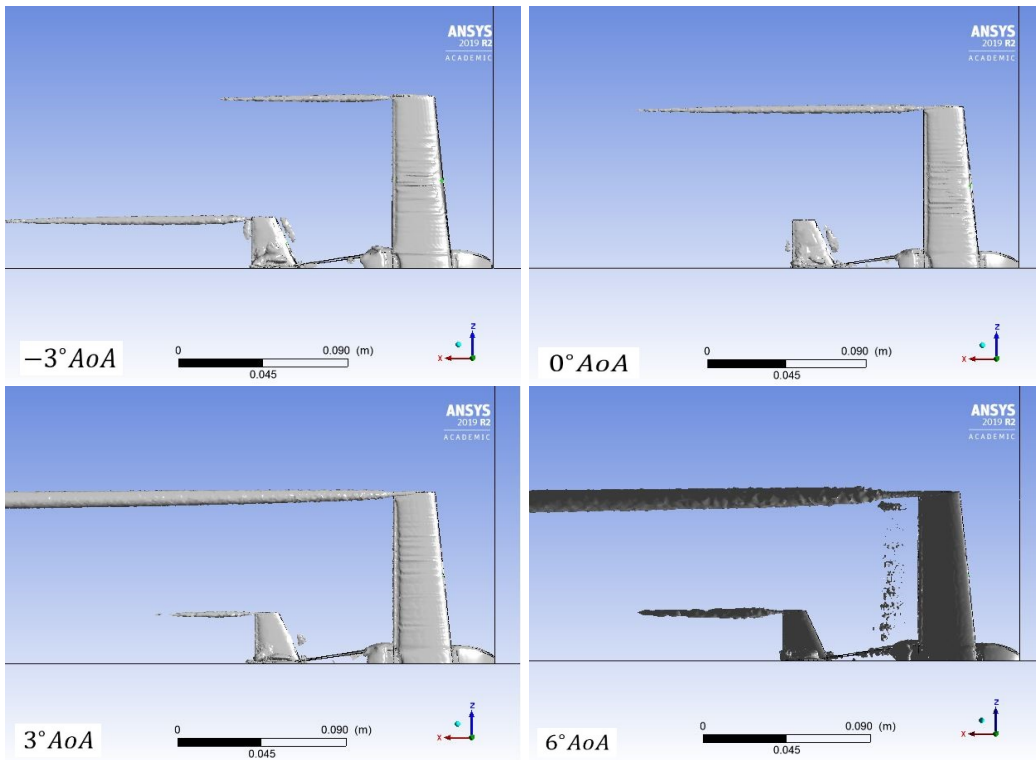

Figure 18: Vortex generation behind the aircraft surfaces

3.6 Horizontal Tail Performance

The horizontal tail performance, with the same airfoil implemented, is being assessed by comparison of the performance parameters as can be observed from Fig. 19. Here, the comparison is made on the basis that separate simulations were performed with just horizontal tail in the fluid domain and the results from this are compared to the performance of horizontal tail used in the aircraft to check how the main wing downwash affects it.

17
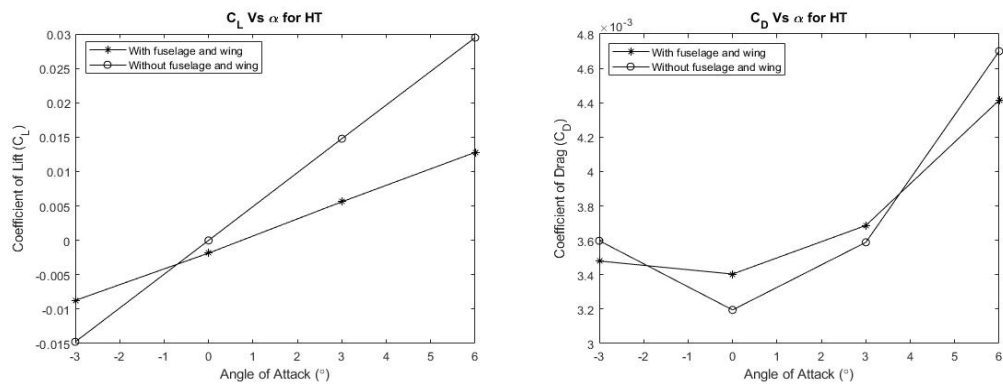
Figure 19: Aerodynamic coefficients comparison on the HT performance

4 Discussion

4.1 Mesh Resolution

It is necessary that the near wall resolution for the mesh is sufficiently fine enough to capture the flow physics occurring inside the boundary layer formed[11], which is the viscous-affected region. Since the aerodynamic characteristics of an aircraft depend on the near-wall flow, therefore it makes it even more important to resolve the near wall physics[12][13]. And this is achieved by observing the $y+$ value over the surface of the aircraft.

Here, it can be observed from Fig. 7 that the mesh resolution at the aircraft surface is made sufficiently fine enough to capture the near wall physics to determine the aerodynamic coefficients properly. Also, the mesh quality is high enough to avoid any discretization errors, which can be observed from Table. 5.

4.2 Solution Stability

For verification purposes, the obtained solution should be checked for convergence. Therefore, to obtain a stable solution for the solution variables, velocity-magnitude is checked for stability purposes at the monitor points, and can be observed from Fig. 8. To ensure that the solution variables remain stable for a longer period of time, the number of iterations for all the simulations is kept high. The drawback of keeping the number of iterations very high is that the computational cost becomes more. But for better accuracy of the results, and with the available computational power, it is made possible to run all the simulations in the given time frame.

Here, it can be observed that the solution variables are sufficiently stable enough to rely on the solution obtained. Also, it has been made sure that the solution stability is obtained for all the simulations being performed here in this study.

4.3 Aircraft Aerodynamic Performance

The aircraft performance is highly affected by the wing-tip vortices and the downwash generated by it. Hence, to have an initial estimate of the aerodynamic performance of the aircraft, a study for the aerodynamic coefficients is studied for various angles of attacks, and can be observed from Fig. 10.

Here, it can be observed from the $C_L - \alpha$ curve that the lift coefficient for the aircraft varies very linearly with the increase in angle of attack, but the rate of increase in the lift coefficient reduces with the increase in the angle of attack. Also, it can observed that has a positive C_L for zero AoA, thereby maintaining enough lift for take-off and cruise conditions. An important factor affecting the effective lift is the choice of the airfoil being implemented for the wings. High cambered airfoils provide more lift when compared to the conventionally used symmetric airfoils.

The force which resists the motion of the aircraft in the forward direction is known as the drag force, which is generated due to various reasons like the skin-friction, pressure and lift-induced drag. These all factors contribute to the total

drag of the aircraft and is quantified using the term - drag coefficient. Here, it can be observed from the Fig. 10 that the drag coefficient of the aircraft increases with the increase in the AoA. The reason behind this is that the contribution of the lift-induced drag increases in comparison to the friction drag at higher AoA's, since the lift coefficient also linearly increases with the increase in AoA. Also, with the increase in AoA, the flow tends to separate, also known as the boundary layer separation, from the wing's trailing edge and this separation point moves towards the leading edge with the increase in AoA. This boundary layer separation causes local low-velocity re-circulation zones, and hence the contribution of the pressure drag due to the re-circulations becomes more significant. Which thereby aids the drag coefficient to increase on an increase in the AoA.

Another factor affecting the increase in the drag is the downwash created by the wingtip vortices on increasing the AoA. The downwash on the wingtips is generated due to the pressure difference acting on the upper and lower surface of the wing. Generally, at the wingtips, the air from the high pressure region curles inwards and upwards to the suction area of the wing, which is the upper surface. Thereby generating the vortical structures, which when leave the wingtip grow and cascade away behind the aircraft. These vortices get stronger and bigger on further increasing the AoA. Thereby affecting the drag on the aircraft.

4.4   Boundary Layer Thickness and Turbulence

The condition expressed in equation 3 is implemented, and on checking for the thickness, the results can be observed from Table. 10. Here, it can be observed that the boundary layer thickness increases downstream of the wing, and this behavior is observed for all AoA's, because as the fluid flow moves downstream, the viscosity of the fluid is responsible to slow more and more fluid layers in the normal direction to the plate, and this phenomenon is known as momentum transfer. This transfer leads to the increase in the boundary layer thickness as we move downstream of the flow[14]. A thicker boundary layer can cause unsteadiness in the flow behavior and thereby causing it to separate from the body and generate separated flow which are generally responsible for the wake areas. The formation of these wakes are responsible to increase the drag on the component with the increase in angle of attack, which can also be observed from Table. 11. Therefore it is necessary to delay the separation of the flow to the very aft of the wing to avoid losing the aerodynamic performance of the component.

Turbulent flows are characterized by occasional formation of intense and localized velocity gradients[15]. To observe these gradients along the normal direction, the following variable is implemented,

$$Velocityu.GradientY$$

Since a turbulence model is being applied here, the solver assumes a turbulent boundary layer throughout, missing out the laminar regions which might occur on the initial stages of boundary layer formation towards the trailing edges of the wing or any other surface in particular. Here, it can be observed from the Fig. 13, that on moving towards the aft side of wing, the curve for the velocity gradient at the wall is more steeper. Due to the random motion of the fluid particles in three-dimensional

interchanges of momentum, a turbulent boundary layer has larger wall velocity gradients and thereby generating very high wall shear stresses locally. It can also be observed that for Line-3, the curve for the gradient is the maximum when compared to the other two lines which are placed at the upstream position comparatively. This indicates that the fluid velocity between the adjacent fluid layer changes rapidly on moving normally away from the wall, and this is the characteristics of the velocity gradient inside the turbulent boundary layer[16][17]. While, the other 2 lines which are placed in the upstream direction have a much smoother gradient away from the wall, indicating less turbulence there. Here, the gradient for the lines upstream is positive at the wall surface, indicating that the flow is still attached to the surface, while the Line-3 has a negative gradient at the wall, indicating that the flow has separated from the surface[18]. This separation becomes more dominant on increasing the AoA, and can clearly be observed from Fig. 13 by observing the gradient at the wall.

The pressure gradient at the trailing edge of the wing is higher for 6° AoA as can be observed from Fig. 15. This high pressure gradient acting in the flow direction induces an inflection point in the flow, which separates the flow as these pressure forces overcome the fluid's inertial forces, and a phenomenon occurs known as the boundary layer separation[19]. Separation causes flow reversal and formation of wakes as observed from Fig. 14, and induces pressure drag affecting the aerodynamic performance of the aircraft. The wake area and the corresponding drag produced can be observed from Table. 11. Here, it can be observed from the table that on increasing the AoA, the flow separation at the wing aft increases and the separation moves upstream and consequently the contribution of the pressure drag compared to the viscous drag is increasing with increase in AoA and also the total drag acting on the wing increases with it. This increase in the pressure drag leads to increase in the total drag acting on the aircraft as can be observed from Fig. 10 and affects the aerodynamic performance of the aircraft for higher angles of attacks.

4.5   Vortices Formation

The vortices generated at the wing-tips can be observed from Fig. 16 and Fig. 17. Here, it can be observed from the streamlines that the wingtip vortices grow in intensity as the AoA increases, which is due to more flow curling back inwards to the suction side of the wing. This vortices grow in size and intensity when move downstream in the flow direction. This curling of the flow causes a downwash effect of the aircraft, and affects the overall lift characteristics of the wing. Also, this curling of vortices also affect the horizontal tail performance by hitting of the air, thereby creating a pitch up moment on the aircraft.

While, to check for the vortical structures leaving from the aircraft surface, a vortex core region has been developed, as can be observed from Fig. 18. Here, the growing of the wingtip vortices can clearly be observed with the increase in AoA. Also, a large vortex region from the horizontal tail for −3° AoA is also observed from the wing tip, which is comparatively stronger when compared to other AoA's.

4.6   Horizontal Tail Performance

The aerodynamic performance of the horizontal tail can be observed from Fig. 19. It can be observed here that the performance of the HT is largely affected by the flow over the wings. Another factor affecting the performance is the vortices leaving the wingtips, which curl up and exert a down force on the HT as observed from Fig. 16 and Fig. 17. And the effect of the curling of the wingtip vortices is larger for higher angles of attacks as can be observed from Fig. 19.

5   Conclusion

With the available resources and the implementation of the necessary CFD approach, a detailed external aerodynamic analysis on the aircraft has been performed with the appropriate parameters. It is observed that on increasing the AoA, the aerodynamic coefficients also increase, but the wake area is also more with higher AoA's. Boundary layer separation at higher angles of attacks is observed, which increase the drag on the aircraft. This can be mitigated by implementing appropriate techniques, i.e., by inducing turbulence in the flow, to delay the separation to the aft of the wing. With the increase in angle of attack, the wingtip vortices grow in size and strength, and can affect the maneuverability of the aircraft. The effect of this vortex formation can be reduced by the utilization of winglets. It is also found that the horizontal tail performance is affected by the wingtip vortices, which can further affect the maneuverability of the aircraft, and this can be avoided with the use of a T-tail instead of a conventional tail configuration as our aircraft has a high-wing mounting, and the wake from the main wing affects the inbound flow to the horizontal tail. Hence, more trimming is required to maintain a stable cruise flight condition.

References

[1] Optimum domain size; 2018. `https://studentcommunity.ansys.com/thread/optimum-domain-size-for-fluid-flow-problems/`.

[2] What is the advantage of hexahedral mesh over tetrahedral elements in finite element analysis using structural analysis?; 2017. `https://www.researchgate.net/post/What_is_the_advantage_of_hexahedral_mesh_over_tetrahedral_elements_in_finite_element_analysis_using_structural_analysis`.

[3] Determining mesh quality; 2019. `https://studentcommunity.ansys.com/thread/determining-mesh-quality/`.

[4] Spalart PR, Allmaras SR. A one-equation turbulence model for aerodynamic flows. Researchgate; 1992.

[5] Versteeg HK, Malalasekera W. An introduction to Computational Fluid Dynamics. 2nd ed. Pearson Education Limited; 2007.

[6] Todorov MD. Determination of the aerodynamic characteristics of a light aircraft using ANSYS workbench and FLUENT software. 2015 01;2015:117–122.

[7] Keating M. Accelerating CFD Solutions Several recent enhancements in ANSYS FlueNt solver capabilities accelerate convergence and reduce solution time, ANSYS;. .

[8] ANSYS FLUENT 12.0 Theory guide; 2012. `https://www.afs.enea.it/project/neptunius/docs/fluent/html/th/node368.htm`.

[9] Airfoil; 1999. `https://web.mit.edu/2.972/www/reports/airfoil/airfoil.html`.

[10] Chernyshenko S, GALLETTIÂ BÂ, IOLLOÂ AÂ, ZANNETTIÂ L. Trapped vortices and a favourable pressure gradient. Journal of Fluid Mechanics. 2003 05;482:235 – 255.

[11] Aftab SMA, Mohd Rafie AS, Razak NA, Ahmad KA. Turbulence Model Selection for Low Reynolds Number Flows. PLOS ONE. 2016 04;11(4):1–15. Available from: `https://doi.org/10.1371/journal.pone.0153755`.

[12] y+ requirement discussion; 2016. `https://www.researchgate.net/post/Do_we_need_to_check_the_y_values_for_SST_K_W_turbulence_model_during_post_processing_and_if_yes_should_the_y_value_be_1_everywhere_on_the_wall`.

[13] Near wall treatment; 2018. `https://studentcommunity.ansys.com/thread/neat-wall-tratment/`.

24

[14] Why the boundary layer thickness for flow over a flat plate continuously increases?; 2016. `https://www.researchgate.net/post/Why_the_boundary_layer_thickness_for_flow_over_a_flat_plate_continuously_increases`.

[15] Buaria D, Pumir A, Bodenschatz E, Yeung PK. Extreme velocity gradients in turbulent flows. New Journal of Physics. 2019 apr;21(4):043004. Available from: `https://doi.org/10.1088%2F1367-2630%2Fab0756`.

[16] On Boundary Layers: Laminar, Turbulent and Skin Friction; 2016. `https://aerospaceengineeringblog.com/boundary-layers/`.

[17] ResearchGate; 2015. `https://www.researchgate.net/post/which_one_offers_biggest_shear_stress_value_than_other_laminar_or_turbulent`.

[18] Sturm H, Dumstorff G, Busche P, Westermann D, Lang W. Boundary Layer Separation and Reattachment Detection on Airfoils by Thermal Flow Sensors. Sensors (Basel, Switzerland). 2012 12;12:14292–306.

[19] Boundary Layer Separation and Pressure Drag; 2016. `aerospaceengineeringblog.com/boundary-layer-separation-and-pressure-drag/`.